J. Fluid Mech. (2025), *vol.* 1016, A1, doi:10.1017/jfm.2025.10243

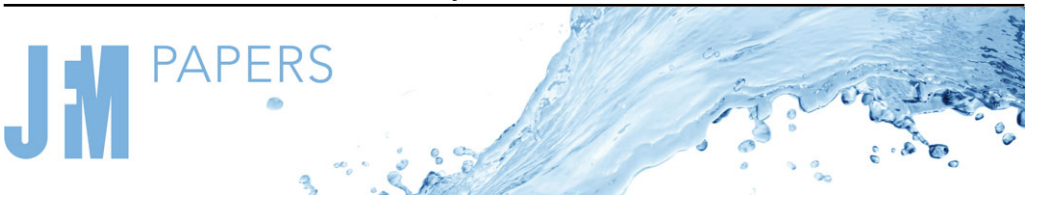

Estimating the skin-friction coefficient in drag-reduced pipe flows of a flexible polymer

Lucas Warwaruk[1], **Satyajit Singh**[1], **Patricio F. Mendez**[2] **and Sina Ghaemi**[1]

[1]Department of Mechanical Engineering, University of Alberta, Edmonton, AB T6G 1H9, Canada

[2]Department of Chemical & Materials Engineering, University of Alberta, Edmonton, AB T6G 1H9, Canada

Corresponding author: Sina Ghaemi, ghaemi@ualberta.ca

(Received 6 April 2024; revised 18 March 2025; accepted 25 April 2025)

In turbulent pipe flows, drag-reducing polymers are commonly used to reduce skin-friction drag; however, predicting this reduction in industry applications, such as crude oil pipelines, remains challenging. The skin-friction coefficient (C_f) of polymer drag-reduced turbulent pipe flows can be related to three dimensionless parameters: the solvent Reynolds number (Re_s), the Weissenberg number (Wi) and the ratio of solvent viscosity (η_s) to zero-shear-rate viscosity (η_0), denoted as β. The function that relates these four dimensionless numbers was determined using experiments of various pipe diameters (D), flow velocities (U) and drag-reducing polyacrylamide solutions. The experiments included measurements of streamwise pressure drop (ΔP) for determining C_f, and measurements of shear viscosity (η) and elastic relaxation time (λ). This experimental campaign involved 156 flow conditions, each characterised by distinct values for C_f, Re_s, Wi and β. Experimental results demonstrated good agreement with the relationship: $C_f^{-1/2} = \widehat{A}\log_{10}(Re_s C_f^{1/2}) + \widehat{B}$, where $\widehat{A} = 27.6(Wi\beta)^{0.346}$ and $\widehat{B} = 122/15 - 58.9(Wi\beta)^{0.346}$. Based on this relationship, onset and maximum drag reduction are predicted to occur when $Wi\beta$ equals 3.76×10^{-3} and 3.40×10^{-1}, respectively. This function can predict C_f of dilute polyacrylamide solutions based on predefined parameters (bulk velocity, pipe diameter, density, solvent viscosity) and two measurable rheological properties of the solution (shear viscosity and elastic relaxation time) with an accuracy of $\pm 9.36\,\%$.

Key words: Drag reduction, turbulent pipe flow, viscoelasticity

1. Introduction

Dissolving a small amount of high-molecular-weight polymers into the turbulent pipe flow of a liquid is a well-established method for reducing skin-friction drag. The most effective drag-reducing polymers are long-chain flexible molecules that form viscoelastic solutions with a large elastic relaxation time (White & Mungal 2008). Although polymers are readily used for drag reduction (DR) in industry applications, such as crude oil pipelines (Burger, Chorn & Perkins 1980), predicting the ability of a given polymer to reduce drag in certain flow conditions is challenging due to the lack of an analytical model. Additionally, numerical simulations of turbulent viscoelastic fluids are computationally expensive and do not map easily to realistic polymer solutions for predicting polymer DR (Xi 2019). Furthermore, DR in polymer-laden pipe flows shows a strong dependency on shear rate; therefore, smaller laboratory experiments with high-shear flows do not translate to the large diameter pipes used in crude oil pipelines, even at similar Reynolds numbers Re (Savins & Seyer 1977). As a result, choosing the right type and amount of polymer to achieve optimal DR in industry is expensive and inefficient. For example, a combination of laboratory-scale testing and field trials was needed for the proper implementation of drag-reducing polymers in the Trans Alaska Pipeline System, which ultimately yielded DR as large as 30 % (Burger *et al.* 1980, 1982).

Early investigations of drag-reducing polymers aimed to establish a relationship between DR and chemical characteristics, such as molecular weight, structure and polymer concentration (Virk 1975). However, it is unreasonable to expect these models can accurately predict DR, considering DR is strongly influenced by flow parameters such as velocity and geometry. Also, the final molecular weight depends on solution preparation, as long-chain polymers often degrade in high-shear conditions (den Toonder *et al.* 1995). Therefore, instead of correlating the chemical properties of polymers with DR, later investigations have focused on establishing a connection between rheological measurements of the solution and DR (Owolabi, Dennis & Poole 2017; Chandra, Shankar & Das 2020).

Inspired by the numerical investigation of Housiadas & Beris (2013), Owolabi *et al.* (2017) demonstrated that the DR of polymer drag-reduced pipe, channel and duct flows was exponentially related to a near-wall Weissenberg number $Wi_\tau = \dot{\gamma}_w \lambda$, where $\dot{\gamma}_w$ is the wall shear rate in the drag-reduced flow and λ is the elastic relaxation time measured from capillary break-up extensional rheology (CaBER). Here, the Weissenberg number is an estimate for the extent polymers are stretched within the flow, and is represented by the product of λ and a characteristic shear rate. Measurements of DR and Wi_τ by Owolabi *et al.* (2017) reasonably collapsed on the proposed exponential trend. On the other hand, later experiments by Chandra *et al.* (2020) demonstrated that the C_f and DR of polymer solutions showed good scaling with $Wi(1-\beta)$, where $Wi = U\lambda/D$ is a bulk Weissenberg number and $\beta = \eta_s/\eta_0$ is the ratio of the solvent viscosity η_s to the zero-shear-rate viscosity of the polymer solution η_0. Here, U is the bulk velocity and D is the pipe diameter.

Although, Owolabi *et al.* (2017) and Chandra *et al.* (2020) demonstrated that DR was strongly related to the Weissenberg number, both works have their respective limitations. Owolabi *et al.* (2017) acknowledged that DR does not depend on Wi_τ alone, but should also depend on the polymer contributions to the viscosity (i.e. β) and the Reynolds number. Furthermore, predicting DR based on Wi_τ is not trivial, because it requires measurements of $\dot{\gamma}_w$ in the drag-reduced flow, which changes depending on Reynolds number, DR and the shear thinning rheology of the solution. On the other hand, Chandra *et al.* (2020) utilised the more easily calculated Wi instead of Wi_τ, and also incorporated β into their scaling. That said, the experiments of Chandra *et al.* (2020) used microtubes with small

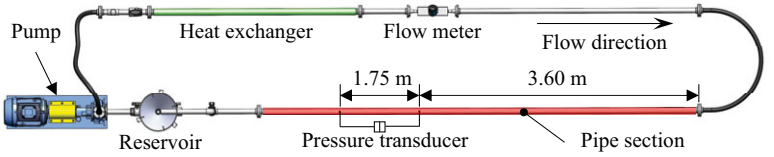

Figure 1. Annotated top view drawing of the recirculating flow loop. The pipe highlighted in red draws attention to the 6 m long interchangeable pipe section.

D (0.5–3 mm) and low Re (3000–4000), much less than those measured in Owolabi *et al.* (2017) and closer to the transitional regime.

To help set up the objective of the present investigation and define the relevant non-dimensional parameters for the polymer drag-reduced, smooth-wall, pipe flows, the dimensional analysis of Buckingham (1914) is employed. The pressure gradient along the streamwise direction of the pipe $\Delta P/\Delta x$ is taken to be the dependent variable. Independent variables relevant to the geometry and speed of the flow, include the pipe diameter D, and the bulk flow velocity U. Independent variables relevant to the properties of a dilute and viscoelastic polymer solution include the density ρ, the solvent viscosity η_s, the zero-shear-rate viscosity η_0 and the polymer relaxation time λ. Utilisation of only these two non-Newtonian parameters assumes that viscoelasticity is the only relevant parameter for DR in the flexible polymer solutions, and neglects other rheological complexities (e.g. shear thinning or finite extensibility). The validity of this assumption will be discussed throughout the analysis. Given the $n = 7$ variables, and $k = 3$ units (mass, length and time), a functional relationship that consists of $n - k = 4$ dimensionless variables can be formed. In this case, the functional relationship is represented as

$$C_f = \psi\,(Re_s,\, Wi,\, \beta), \tag{1.1}$$

where the skin-friction coefficient $C_f = (\Delta P/\Delta x) \cdot D/(2\rho U^2)$, the solvent Reynolds number is $Re_s = \rho U D/\eta_s$, the viscosity ratio is $\beta = \eta_s/\eta_0$ and the Weissenberg number is $Wi = U\lambda/D$. The objective of the upcoming experiment is to identify the relationship ψ, that can predict C_f based on Re_s, Wi and β. These dimensionless parameters depend on known or measured quantities of the flow velocity, geometry and fluid properties.

Experimental measurements using a drag-reducing flexible polymer are used to establish the relationship (1.1). The experiments include measuring the streamwise pressure gradient in the straight pipe section of a recirculating flow loop across a wide range of conditions, including different diameters D, velocities U, polymer concentrations c, solvent viscosity η_s and degradation conditions. Each polymer solution possesses unique values of η_0 and λ obtained from measurements of shear and extensional rheology. Finally, a dimensionless relationship is established to predict C_f of polymer drag-reduced pipe flows, provided Wi, β, and Re are known *a priori*.

2. Experimental methodology

2.1. *Turbulent pipe flow*

The turbulent pipe flow of drag-reducing solutions of the flexible polymer polyacrylamide (PAM) were evaluated in a recirculating flow loop shown schematically in figure 1. The selection of PAM for these experiments was due to its widespread use as a water-soluble drag reducer and its higher resistance to chain scission induced by flow shear (Pereira & Soares 2012; Soares *et al.* 2015). Three pipe sections with different inner diameters D of 26.7, 41.3 and 52.5 mm, were installed and tested within the red highlighted region of the

D (mm)	$\dot{m}$ (kg s^{-1})	U (m s^{-1})	Re_s	c (ppm)
26.7	1.26, 1.47, 1.68 1.89, 2.10	2.25, 2.63, 3.01 3.39, 3.77	60 000; 70 000; 80 000; 90 000; 1 00 000	0, 50
41.3	1.93, 2.25, 2.57 2.89, 3.21	1.45, 1.69, 1.93 2.17, 2.41	60 000; 70 000; 80 000; 90 000; 1 00 000	0, 50, 100, 150
52.5	2.48, 2.89, 3.30 3.71, 4.12	1.15, 1.34, 1.53 1.72, 1.91	60 000; 70 000; 80 000; 90 000; 1 00 000	0, 50

Table 1. List of prescribed flow conditions for each pipe section with diameter D, PAM concentrations c and a pure water solvent $\eta_s = 1.0$ mPa s and $\rho = 998$ kg m^{-3}.

flow loop shown in figure 1. All other piping within the flow loop had an inner diameter of 52.5 mm. Concentric reducers were used to gradually transition the pipe section to smaller diameters when required. A centrifugal pump (LCC-M 50-230, GIW Industries Inc.) was used to circulate the fluid within the loop and a Coriolis flow meter (Micro Motion F-Series, Emerson Electric Co.) was used to measure the mass flow rate $\dot{m}$. A proportional-integral-derivative controller was used to maintain a constant $\dot{m}$ by adjusting the rotational speed of the pump using a variable frequency drive. A thermocouple and shell-and-tube heat exchanger were used to measure and maintain a constant fluid temperature of 20 °C $\pm$ 0.5 °C across all experimental trials.

For each pipe diameter D, five different $\dot{m}$ were considered, as listed in table 1. The bulk velocity was determined according to $U = \dot{m}/(\rho a)$ and listed in table 1, where $a = \pi D^2/4$ is the cross-sectional area of the pipe and ρ is the density. The solvent Reynolds number Re_s is listed in table 1 for each pipe. The pressure drop ΔP was measured utilising a differential pressure transducer (DP-15, Validyne Engineering) along a streamwise distance of $\Delta x = 1.75$ m (corresponding to approximately $33.3D$ to $65.5D$, depending on the pipe diameter). The most upstream pressure port was positioned 3.6 m downstream from the inlet of each pipe section (equivalent to $68.6D$ to $134.8D$), as illustrated in figure 1, to ensure a fully developed flow. Measurements of ΔP were collected at a sampling rate of 1 Hz using a National Instruments data acquisition system. For each $\dot{m}$, measurements of ΔP were collected for 5 min and then averaged over time.

The chosen PAM polymer (6030S, SNF Floerger) had a molecular weight M_w of 30–35 MDa. One concentration c of PAM, equal to 50 ppm, was tested in all pipe sections with different D. However, aqueous PAM solutions with larger c of 100 and 150 ppm were also tested, but only in the $D = 41.3$ mm pipe. In addition to pure water with $\eta_s = 1.0$ mPa s and $\rho = 998$ kg m^{-3}, two glycerol/water solutions were also examined in the $D = 26.7$ mm pipe. One solvent was a 25 % glycerol/water solution, with $\eta_s = 1.8$ mPa s and $\rho = 1089$ kg m^{-3}, and the other was a 35 % glycerol/water solution, with $\eta_s = 2.5$ mPa s and $\rho = 1113$ kg m^{-3}. Flow conditions for these solvents are listed in table 2. Values of η_s were measured from steady shear rheology in a torsional rheometer. The mass flow rates $\dot{m}$ for these conditions are manipulated such that they achieve three similar Re_s as those for pure water with $\eta_s = 1.0$ mPa s listed in table 1 for the same diameter of $D = 26.7$ mm. One PAM concentration of $c = 50$ ppm was tested with these more viscous glycerol/water solvents. Baseline measurements of Re_s versus C_f for the different solvents, without PAM, are shown in Appendix A, and all demonstrate good agreement with the Prandtl's friction law of $C_f^{-1/2} = 4.0 \log_{10}(Re_s C_f^{1/2}) - 0.4$ for Newtonian turbulent pipe flow.

In order to obtain solutions with lower DR, the PAM fluids were intentionally degraded by increasing the rotational speed of the pump for different amounts of time. An example

Solvent	$\dot{m}$ (kg s^{-1})	U (m s^{-1})	Re_s	c (ppm)	η_s (mPa s)	ρ (kg m^{-3})
25 % glycerol/water	2.54, 2.97 3.39	4.18, 4.88 5.56	70 000; 80 000; 90 000	0, 50	1.8	1089
35 % glycerol/water	3.70, 4.29 4.87	5.93, 6.88 7.82	70 000; 80 000; 90 000	0, 50	2.5	1114

Table 2. List of flow conditions for additional tests performed with more viscous solvents, the first being a 25 % glycerol/water solution and the second being a 35 % glycerol/water solution. Experiments tested here were performed in the $D = 26.7$ mm diameter pipe.

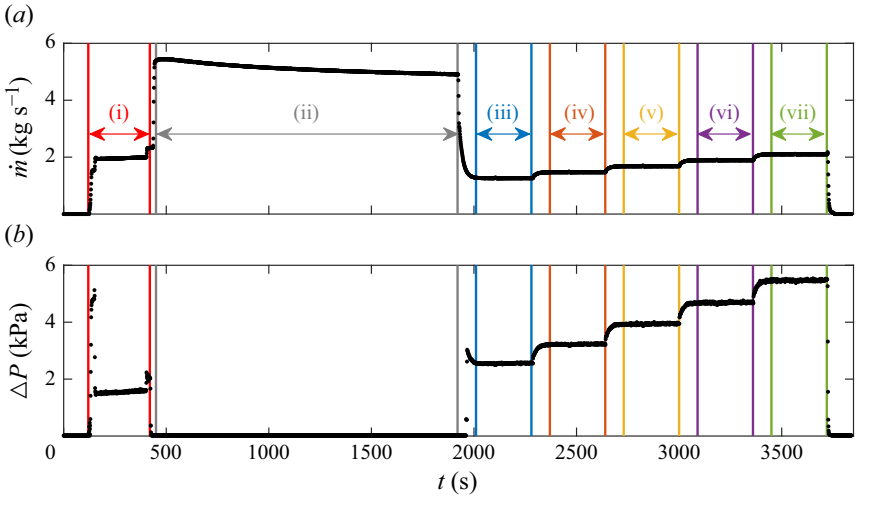

Figure 2. A sample plot of (a) mass flow rate $\dot{m}$ and (b) streamwise pressure drop ΔP versus time t for a 50 ppm PAM solution degraded within the $D = 26.7$ mm pipe. Vertical lines of similar colour represent the bounds for averaging windows, where measurements of $\dot{m}$ and ΔP were averaged.

of the degradation procedure for a 50 ppm PAM solution in the $D = 26.7$ mm pipe, with a pure water solvent ($\eta_s = 1.0$ mPa s) is shown in figure 2. Figure 2(a) shows the time series of mass flow rate $\dot{m}$ with respect to time t, and figure 2(b) demonstrates the time series of pressure drop ΔP versus t for the same experiment. Coloured vertical lines in figure 2 represent the bounds of different stages of the experiment. Each stage is labelled with a roman numeral in figure 2(a) that increases chronologically with t. Prior to the experimental trial, a 15 l concentrated master solution was prepared. In stage (i), the master solution is added to the flow loop and circulated for 300 s at a constant pump rotational speed of 300 rpm, mixing and diluting the solution to the desired c. Shortly after mixing, the rotational speed of pump is increased to 1200 rpm and the solution is intentionally degraded. This degradation phase, labelled stage (ii) and bounded by grey lines in figure 2, was 1470 s for the experiment shown in figure 2. The exact duration of stage (ii) was manipulated day to day to achieve drag-reduced flows with different C_f values and polymer rheology. As an exception, to achieve C_f values near the maximum DR, the solutions were not degraded, and stage (ii) was omitted. In stage (ii) of figure 2(a), polymer degradation causes $\dot{m}$ to decrease with respect to t, when the pump is maintained at a constant rotational speed. Values of ΔP are large in stage (ii) and would exceed the range of the differential pressure transducer. To avoid damaging the transducer during

stage (ii), the pressure sensor is isolated from the flow loop using valves; hence the appearance of $\Delta P = 0$ in stage (ii) of figure 2(*b*). After degradation, the rotational speed of the pump is reduced and the valves that feed the pressure transducer are re-opened. The $\dot{m}$ is then set to the lowest value of 1.26 kg s^{-1} for the $D = 26.7$ mm pipe listed in table 1 and held at that $\dot{m}$ for $\Delta t = 300$ s. The proportional-integral-derivative controller is used to manipulate the rotational speed of the pump and maintain a constant $\dot{m}$ for the 300 s duration. Stage (iii), bounded by blue lines in figure 2, is a 270 s window where $\dot{m}$ and ΔP were averaged over t; 30 s of data were neglected to avoid any transient development in the flow. The resulting average values of $\dot{m}$ and ΔP are then used in the calculation of the dimensionless numbers such as C_f, Wi and Re_s. From stages (iv) to (vii), $\dot{m}$ was increased sequentially using the values listed in table 1 for $D = 26.7$ mm. This procedure is the same for the $D = 41.3$ and $D = 52.5$ mm pipes, albeit with different prescribed values of $\dot{m}$ for stages (iii) to (vii), as listed in table 1. This degradation procedure was used to produce eight, eleven and six different degraded 50 ppm PAM solutions for the $D = 26.7$, 41.3 and 52.5 mm pipes, respectively. While for the 100 and 150 ppm PAM solutions, three and two different degraded solutions were considered, respectively, within the $D = 41.3$ mm pipe. Only fresh PAM solutions (i.e. with no degradation) were tested for the two glycerol/water solvents with properties listed in table 2. Overall, this investigation considered drag-reduced pipe flows with three D, five $\dot{m}$, and 32 different PAM solutions (three c, three solvents η_s and two to eleven different amounts of degradation), thus producing a total of 156 unique trials with different rheology and C_f.

2.2. *Fluid rheology*

For each PAM solution, and at each $\dot{m}$, fluid samples were collected for shear and extensional rheology measurements from the flow loop half-way through the 270 s data collection intervals labelled (iii) to (vii) in figure 2. The steady shear viscosity η with respect to shear rate $\dot{\gamma}$ was measured for each sample using a single-head torsional rheometer (DHR-2, TA Instruments) equipped with a double-gap concentric cylinder geometry. Each curve of η versus $\dot{\gamma}$ is fit with the model of Cross (1965)

$$\frac{\eta - \eta_\infty}{\eta_0 - \eta_\infty} = \frac{1}{1 + (K\dot{\gamma})^m}, \tag{2.1}$$

where η_∞ is the infinite-shear-rate viscosity, η_0 is the zero-shear-rate viscosity, K is the consistency and m is the flow index. Sample measurements of shear viscosity η versus shear rate $\dot{\gamma}$ are shown in figure 3(*a*) for seven $c = 50$ ppm PAM solutions with different amounts of degradation. At low $\dot{\gamma}$, measurements of η are neglected due to the low torque limitation ($M < 600$ nN m) of the device, as indicated by the solid black line on the left side of figure 3(*a*). At larger $\dot{\gamma}$, measurements of η demonstrate an abrupt increase due to the inception of Taylor vortices at a Taylor number Ta of 1700 and indicated by the solid black line on the right side of figure 3(*a*). The coloured lines represent Cross model (Cross 1965) fits represented by (2.1). Figure 3(*a*) demonstrates that as the 50 ppm PAM solutions degrade, η decreases for all $\dot{\gamma}$. Furthermore, η_0 demonstrates a notable reduction with increasing amounts of degradation; therefore $\beta = \eta_s/\eta_0$ should increase as PAM solutions degrade. In this case, for the given 50 ppm PAM solutions, β increased from 0.56 to 0.87 with increasing amounts of degradation. For the 100 ppm PAM solutions β was between 0.5 and 0.7, while the 150 ppm PAM solutions had β between 0.2 and 0.5.

Considering the polymer solutions are shear thinning, with shear rheograms described well by (2.1), some doubt is cast on the validity of the assumptions used in § 1 to arrive at ψ of (1.1). Given the polymers are shear thinning, questions arise as to why K, m or η_∞ are not included in (1.1). Although shear thinning has been shown to cause DR

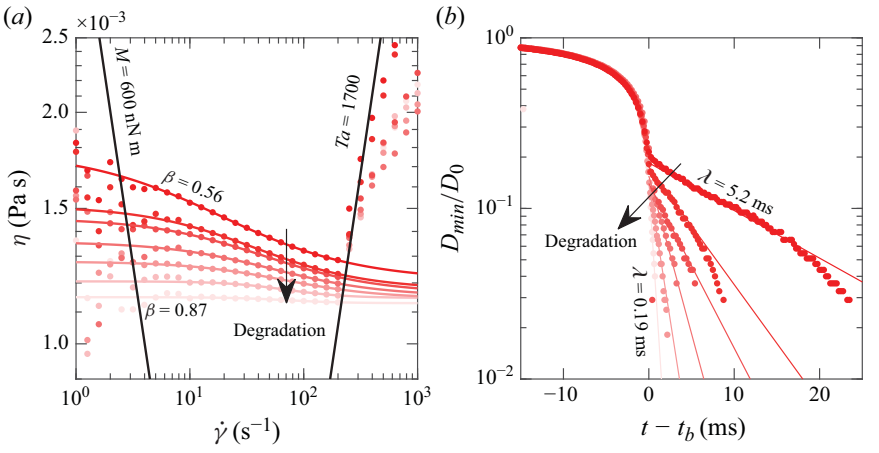

Figure 3. Plots of (*a*) steady shear viscosity with respect to shear rate and (*b*) filament diameter versus time from liquid dripping extensional rheometry. Solid lines in (*a*) are fits using (2.1). Solid lines in (*b*) are fits using (2.2).

(Singh, Rudman & Blackburn 2017; Arosemena *et al.* 2021), its contributions to DR are assumed to be minimal compared with viscoelasticity. Drag reduction using a inelastic Carreau shear thinning constitutive models was investigated using turbulent channel flow direct numerical simulation (DNS) by Arosemena *et al.* (2021). Despite large amounts of shear thinning, with $\eta_\infty/\eta_0 = 1 \times 10^{-3}$, Arosemena *et al.* (2021) reported only a small DR percentage of 10 %. Given the smallest η_∞/η_0 among all of the present drag-reducing PAM solutions is 0.36, which is much closer to unity than that used by Arosemena *et al.* (2021), it is expected that shear thinning does not contribute significantly to C_f in these fluids.

Liquid dripping extensional rheology was used to determine λ for each PAM solution (Deblais *et al.* 2020; Rajesh, Thiévenaz & Sauret 2022). Here, a droplet of each PAM solution is expelled from a blunt end nozzle with an outer diameter of $D_0 = 1.27$ mm, using a syringe pump with a flow rate of 0.02 ml min^{-1}. As the droplet is expelled from the nozzle, a liquid bridge forms between the droplet and the outlet of the nozzle. A high-speed camera (NOVA S9, Photron Inc.) and light emitting diode were used to record images of the minimum diameter D_{min} of the liquid bridge with respect to time t. Viscoelastic polymer solutions tend to exhibit elasto-capillary (EC) thinning, where D_{min}/D_0 closely resembles an exponential function of the form

$$\frac{D_{min}}{D_0} = C \exp\left(-\frac{t - t_b}{3\lambda}\right). \tag{2.2}$$

Here, C is a fitting constant, t_b is an inertial break-up time and λ is the elastic relaxation time (Anna & McKinley 2001). For each sample, extensional rheology measurements were repeated three times. The λ of each solution was taken to be the average of the three values of λ derived from the fits of (2.2). Sample measurements of extensional rheology, given by D_{min}/D_0 with respect to $t - t_b$, are shown in figure 3(*b*) for the same PAM solutions shown in figure 3(*a*) with different amounts of degradation. For $t > t_b$ the PAM solutions exhibit EC thinning, where D_{min}/D_0 resembles (2.2). In the EC regime, λ tends to be smaller for PAM solutions that experience larger amounts of degradation. In this case, the 50 ppm solutions shown in figure 3(*b*) have a λ that reduces from 5.2 to 0.19 ms with increasing amounts of degradation. Regardless of the concentration c, PAM solutions that

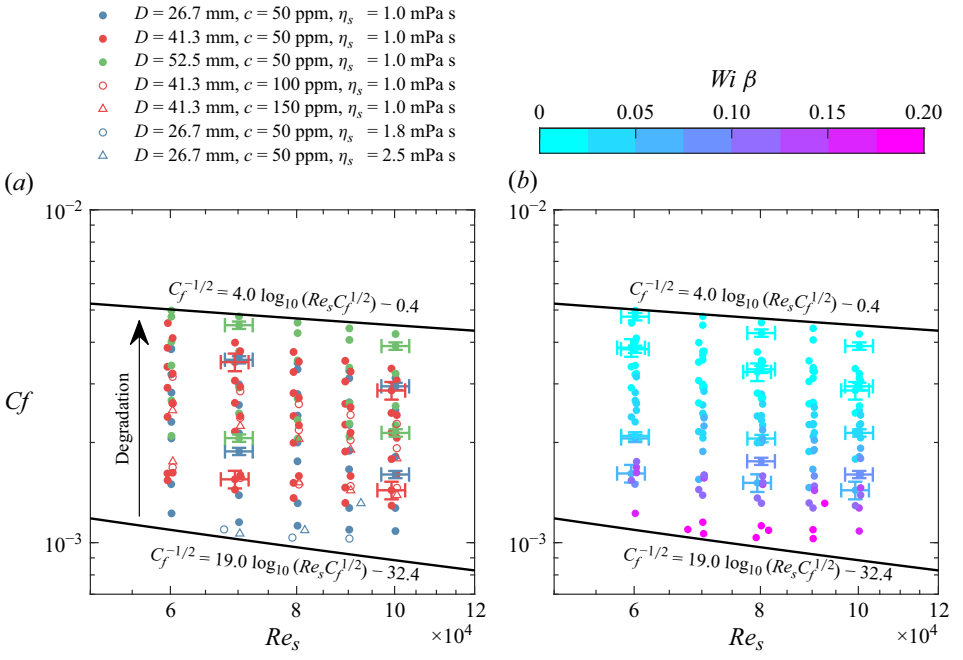

Figure 4. The skin-friction coefficient as a function of solvent viscosity Reynolds number. The upper and lower black lines are the C_f for Newtonian turbulent pipe flow and MDR (Virk *et al.* 1970), respectively.

experience more mechanical degradation tend to have lower values of λ, similar to that shown previously in Owolabi *et al.* (2017) using CaBER measurements of λ. That said, λ tends to be overall larger for solutions with greater c.

The uncertainty in the measurements of $\dot{m}$ and ΔP consist of systematic uncertainties, prescribed by the sensor manufacturer, and random uncertainties, established from the repeatability in the measurements of $\dot{m}$ and ΔP for water. The relative uncertainty in η_0 was conservatively assessed to be $\pm 4.0\,\%$ for all PAM solutions. Uncertainty in λ was assumed to be the range in the thrice-repeated measurements of λ from liquid dripping extensional rheology. Using these estimates, the uncertainty in the dimensionless variables was assessed from propagation of uncertainty (Wheeler & Ganji 2010), and are represented by error bars in all figures to follow. A detailed discussion of the measurement uncertainties is provided in Appendix A.

3. Skin-friction scaling

Plots of C_f versus Re_s are shown in figure 4(*a*) for all 156 pipe flow measurements of PAM with different D, $\dot{m}$, c, η_s and degradation conditions. Markers are coloured according to D, while marker symbols correspond to different c and η_s as indicated by the legend above figure 4(*a*). Figure 4(*a*) demonstrates that the measurements cover a wide range of C_f values, that fall between the C_f versus Re distributions for Newtonian turbulent pipe flows according to Prandtl's friction law of $C_f^{-1/2} = 4.0\log_{10}(Re_s C_f^{1/2}) - 0.4$ and maximum drag reduction (MDR) according to $C_f^{-1/2} = 19.0\log_{10}(Re_s C_f^{1/2}) - 32.4$ (Virk, Mickley & Smith 1970). As the PAM solutions are degraded, C_f increases for a given Re_s, as annotated in figure 4(*a*). Note, that typically Re_s is not used in plots of C_f for polymer drag-reduced flows; rather, a Reynolds number based on a near-wall viscosity

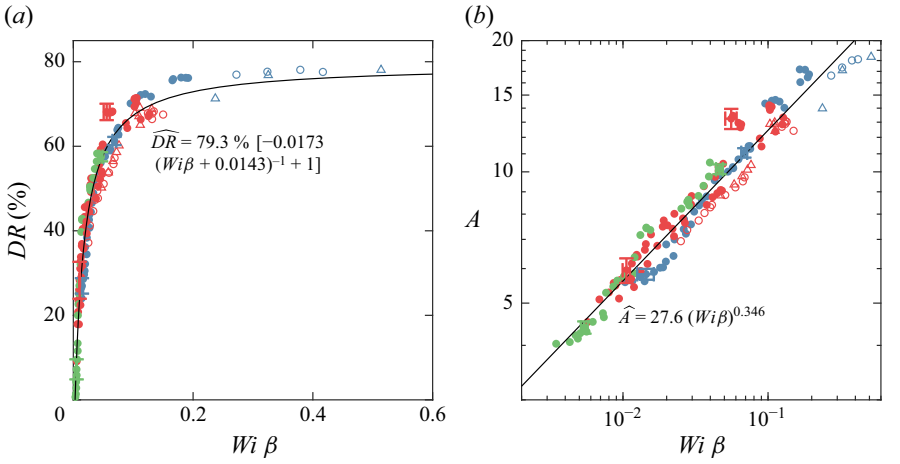

Figure 5. Plots of (*a*) DR versus $Wi\beta$ and (*b*) A versus $Wi\beta$ for the polymeric flows with different D and c. The black lines in (*a*,*b*) represent the fit functions labelled on each plot. Marker symbols and colours are the same as those shown in figure 4(*a*).

$Re_w = \rho U D/\eta_w$ is used (Xi 2019), where η_w is the near-wall viscosity. Different definitions of the Reynolds number, including Re_w and $Re_0 = \rho U D/\eta_0$, are explored later in § 4 of the manuscript.

Figure 4(*b*) shows a plot of C_f versus Re_s, with markers coloured according to each fluid's respective value of $Wi\beta$. The Wi represents the extent to which the polymers are stretched based on the bulk shear rate U/D. In general, a higher Wi indicates greater polymer stretching, which is expected to result in a lower C_f, establishing an inverse relationship. However, this approximation of Wi, derived in § 1, does not account for the effect of polymers on viscosity. As inferred from figure 3, PAM solutions with higher λ (and thus higher Wi) exhibit greater viscosity, which leads to a smaller β. Since this smaller β contributes to a larger C_f, which is also an inverse relationship, Wi is multiplied by β to compensate for the viscosity effect. This is confirmed in figure 4(*b*) showing that C_f decreases as $Wi\beta$ increases for a given Re_s. Flows with small values of $Wi\beta$, close to zero, have values of C_f close to the Newtonian skin-friction correlation, while $Wi\beta$ in excess of 0.2 produce values of C_f that approach MDR. We acknowledge that use of $Wi\beta$ is in contradiction with the prior work of Chandra *et al.* (2020), who demonstrated that C_f scales with $Wi(1-\beta)$. Scaling of C_f with $Wi(1-\beta)$ is discussed in greater detail in § 5.

A DR percentage DR is often used to estimate the reduction in C_f of each polymer solution relative to Newtonian turbulence (Owolabi *et al.* 2017; Xi 2019). Here, the DR percentage of each polymer drag-reduced pipe flow is defined by the equation,

$$DR = \left(1 - \frac{C_f}{C_{f,N}}\right) \times 100\,\%, \tag{3.1}$$

where $C_{f,N}$ is a Newtonian skin-friction coefficient at a similar Re_s (or $\dot{m}$) following Prandtl's friction law. Uncertainty in DR propagates from the errors in C_f, discussed in Appendix A, and is represented by error bars in plots of DR that follow. Other definitions of DR, using $C_{f,N}$ at a similar Re_0 and Re_w as the polymeric flows, are also explored later in § 5.

Figure 5(*a*) demonstrates DR as a function of $Wi\beta$ for all polymer solutions with different c and D. Values of DR show good consistency with one another when plotted with respect to $Wi\beta$, and are well represented by an inverse relationship

$\widehat{DR} = 79.3\,\%[-0.0173(Wi\beta + 0.0143)^{-1} + 1]$. Here, the hat symbol $\widehat{\cdots}$ is used to represent a prediction based on a fit of the measurements. This inverse relationship was chosen because it predicts an onset DR ($DR = 0\%$), and an asymptotic value of DR, corresponding roughly to the limit of MDR in the range of Re_s considered. Based on the fit of $\widehat{DR}$, DR commences when $Wi\beta$ exceeds 3.00×10^{-3}, and DR asymptotically saturates to 79.3 %. The equation for $\widehat{DR}$ fits the measurements well, given a coefficient of determination $R^2 = 1 - \sum_{n=1}^{N}(DR_n - \widehat{DR}_n)^2 / \sum_{n=1}^{N}(DR_n - \langle DR \rangle)^2$ of 0.954. Here, n is a sample measurement, $N = 156$ is the total number of measurements and angle brackets $\langle \cdots \rangle$ represent the average of the quantity contained within the brackets.

Although DR shows good scaling with $Wi\beta$, the proposed inverse equation has some limitations. Notably, the asymptotic limit of $\widehat{DR}$ corresponding to MDR is only expected to apply for the range of Re_s measured here. This is because the skin-friction equation for Newtonian turbulence and MDR diverge with increasing Re_s, and the value of DR corresponding to MDR increases with Re_s. To alleviate this concern, a new variable A is used to describe the proximity of C_f for each drag-reduced flow to the skin-friction coefficient for Newtonian turbulence and MDR. Here, A is the slope of C_f and Re_s in Prandtl–von Kármán coordinates according to

$$C_f^{-1/2} = A \log_{10}(Re_s C_f^{1/2}) + B, \tag{3.2a}$$

$$B = \frac{122}{15} - \frac{32A}{15}, \tag{3.2b}$$

where B is the intercept of $C_f^{-1/2}$ at $Re_s C_f^{1/2} = 1$. Note that, when $A = 4.0$ and 19.0, (3.2) produces the skin-friction correlations for Newtonian turbulence and MDR, respectively. Here B, represented by (3.2*b*), is defined such that all values of A produce lines of C_f versus Re_s that pass through the point of intersection between the lines for Newtonian turbulence and MDR. Values of A are determined for each flow based on their respective value of C_f and Re_s and from rearranging (3.2), as $A = (C_f^{-1/2} - 122/15)/(\log_{10}(Re_s C_f^{1/2}) - 32/15)$. Therefore, each measured value of C_f and Re_s, shown in figure 4(*a*), has a corresponding value of A based on (3.2). Considering all values of C_f for the polymer drag-reduced flows are less than Prandtl's friction law, but greater than MDR – as demonstrated in figure 4(*a*) – it is expected that A will be bounded between 4.0 and 19.0.

A plot of A versus $Wi\beta$ for each flow with known C_f and Re_s values, is shown in figure 5(*b*). As predicted, values of A are between 4.0 and 19.0, corresponding to Newtonian turbulence and MDR, respectively. When plotted with respect to $Wi\beta$, values of A show good consistency with one another for the flows of different D and c, and are accurately described by the power-law function $\widehat{A} = 27.6(Wi\beta)^{0.346}$. The R^2 of this fit is 0.949, which is comparable to that of $\widehat{DR}$. However, unlike the inverse function of $\widehat{DR}$, the function $\widehat{A}$ enables a more obvious prediction of DR onset and MDR, which would occur where $\widehat{A} = 4$ and 19, respectively. Based on the power-law function of $\widehat{A}$ versus $Wi\beta$, DR onset would occur at $Wi\beta = 3.76 \times 10^{-3}$, not too dissimilar from the $Wi\beta = 3.00 \times 10^{-3}$ predicted by $\widehat{DR}$, and MDR would occur at $Wi\beta = 3.40 \times 10^{-1}$. Substituting $\widehat{A}$ for A in (3.2), provides an equation for the skin-friction coefficient as a function of Re_s, Wi and β; in other words, the function ψ, as per (1.1). The function is represented as

$$\widehat{C_f}^{-1/2} = \widehat{A} \log_{10}(Re_s \widehat{C_f}^{1/2}) + \widehat{B}, \tag{3.3a}$$

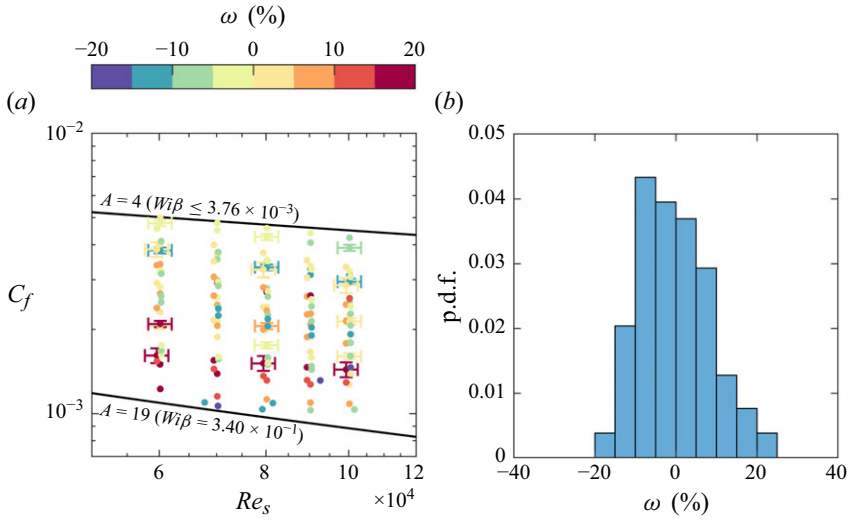

Figure 6. Plot of (*a*) C_f versus Re_s with lines and markers coloured based on A and $\widehat{A}$ respectively, and (*b*) p.d.f. of the per cent difference between $\widehat{C_f}$ and C_f, or ω, for each flow.

where

$$\widehat{A} = 27.6(Wi\beta)^{0.346}, \tag{3.3b}$$

and

$$\widehat{B} = 122/15 - 58.9(Wi\beta)^{0.346}, \tag{3.3c}$$

and $\widehat{C_f}$ represents the predicted value of skin-friction coefficient based on Re_s, Wi and β. As a final simplification, the implicit function of (3.3*a*) can be made explicit through use of the zeroth branch of the Lambert function (Goudar & Sonnad 2003). Therefore, (3.3*a*) can be equally represented as

$$\widehat{C_f}^{-1/2} = \frac{\widehat{A}}{\ln(10)} \mathcal{W}\left[\frac{Re_s \ln(10)}{\widehat{A}} \exp\left(\frac{\widehat{B}\ln(10)}{\widehat{A}}\right)\right], \tag{3.4}$$

where $\mathcal{W}$ is the Lambert function, which is the inverse operation of $f(w) = w\exp(w)$. Here, w is an arbitrary dependent variable. In other words, the Lambert function can be expressed as, $w = \mathcal{W}[w\exp(w)]$.

A per cent difference between $\widehat{C_f}$ and C_f, equal to $\omega = (\widehat{C_f} - C_f)/C_f \times 100\,\%$, is also used to evaluate the accuracy of (3.3). Figure 6(*a*) demonstrates C_f versus Re_s, similar to figure 4(*a*), however, with markers coloured according to values of ω. Large values of ω appear to typically occur at lower C_f or larger DR and $Wi\beta$. One condition in particular with C_f between 1×10^{-3} and 2×10^{-3}, corresponding to the flow with $D = 41.3$ mm and $c = 50$ ppm, shows values of ω near 20 % for all Re_s, perhaps highlighting an anomalous test day. The probability density function (p.d.f.) of ω is shown in figure 6(*b*). The p.d.f. in ω appears to be slightly skewed to more positive values with a median of $-0.332\,\%$ and a mean of $0.318\,\%$. Values of ω vary between $\pm 20\,\%$, as demonstrated by the extents of the p.d.f. shown in figure 6(*b*). An approximate estimate for the accuracy of the prediction (3.3) is assumed to be the standard deviation in ω, which is $9.36\,\%$.

4. Reynolds number definition

Use of Re_s is not typical when considering polymer drag-reduced pipe flows (Xi 2019); generally, the enhanced viscosity of the polymer solutions needs to be taken into account. For that reason, the influence of different Reynolds number definitions are discussed in this section. Figure 7 demonstrates the skin-friction scaling for the two other definitions of the Reynolds number; $Re_0 = \rho U D/\eta_0$ and $Re_w = \rho U D/\eta_w$. Marker colours and symbols, that represent the polymer drag-reduced flows of different D and c, are the same as those defined earlier in figure 4(*a*).

Figure 7(*a*) demonstrate C_f versus Re_0. Considering $\eta_0 > \eta_s$, values of Re_0 are lower than Re_s shown in figure 4(*a*). The PAM solutions with $c = 100$ and $c = 150$ ppm have lower Re_0 values than most of the $c = 50$ ppm flows, due to their much larger η_0. In some instances, values of C_f and Re_0 for the 150 ppm solution fall slightly below the MDR asymptote, calculated based on Re_0. Figure 7(*b*) demonstrates the DR percentage of the polymer drag-reduced flows evaluated according to (3.1), but with respect to a Newtonian skin-friction coefficient $C_{f,N}$ at a similar Re_0. This DR percentage is defined as DR_0. Despite the difference between DR and DR_0, values of DR_0 appear to follow a similar inverse relationship; in this case DR_0 is well predicted by the function $\widehat{DR}_0 = 82.9\,\%[-0.0167(Wi\beta + 0.0142)^{-1} + 1]$. The coefficient of determination R^2 of the function $\widehat{DR}_0$ is 0.958, which is slightly better than that of $\widehat{DR}$. Figure 7(*c*) demonstrates the parameter A_0, defined from rearranging (3.2), but with Re_0 in lieu of Re_s. Similar to A, values of A_0 faithfully follow a power-law trend with respect to $Wi\beta$, but represented by $\widehat{A}_0 = 37.0(Wi\beta)^{0.398}$. The prediction $\widehat{A}_0$ has an $R^2 = 0.926$ that is marginally worse than the R^2 of 0.949 for $\widehat{A}$. Certain values of A_0 also exceed 19 (corresponding to MDR), particularly at larger c and lower D, hinting that Re_0 is not an ideal Reynolds number definition for the flows.

Figure 7(*d*) shows C_f versus a Reynolds number Re_w based on the near-wall viscosity η_w. Here, η_w is derived using the Cross model (2.1) coupled with measurements of the wall shear stress $\tau_w = (D/4)\Delta P/\Delta x$, which can be equally represented as $\tau_w = \eta_w \dot{\gamma}_w$, where $\dot{\gamma}_w$ is the near-wall shear rate. This Reynolds number definition Re_w is typically used in most investigations of polymer drag-reduced flows and is therefore, important to consider (Xi 2019). Generally, $\eta_0 > \eta_w > \eta_s$ and Re_w tends to be lower than Re_s, but larger than values of Re_0 – as seen when comparing figure 4(*a*) with figures 7(*a*) and 7(*d*). The DR percentage DR_w and the slope parameter A_w based on Re_w, shown in figure 7(*e*,*f*), respectively, demonstrate similar trends as those seen for DR and A, with subtle differences in value and the quality of fit. For example, the function $\widehat{A}_w$ has a better data collapse than $\widehat{A}$ and $\widehat{A}_0$, with an R^2 of 0.964, implying Re_w is the most appropriate Reynolds number definition. That said, for the sake of predicting DR or C_f, Re_s is suitable; since the wall viscosity η_w is not known *a priori*.

5. Previous correlations of drag reduction and viscoelastic rheology

The most relevant rheological correlation of DR and elastic flow features was performed by Owolabi *et al.* (2017). As discussed in § 1, Owolabi *et al.* (2017) correlated DR with a near-wall Weissenberg number $Wi_\tau = \lambda \dot{\gamma}_w$, where $\dot{\gamma}_w$ is a wall shear rate estimated from measurements of τ_w from ΔP and shear rheograms. Owolabi *et al.* (2017) proposed that DR should scale with Wi_τ according to

$$DR = 2C_1 \left(\frac{1}{1 + \exp(Wi_c - Wi_\tau)} - Wi_c \right), \tag{5.1}$$

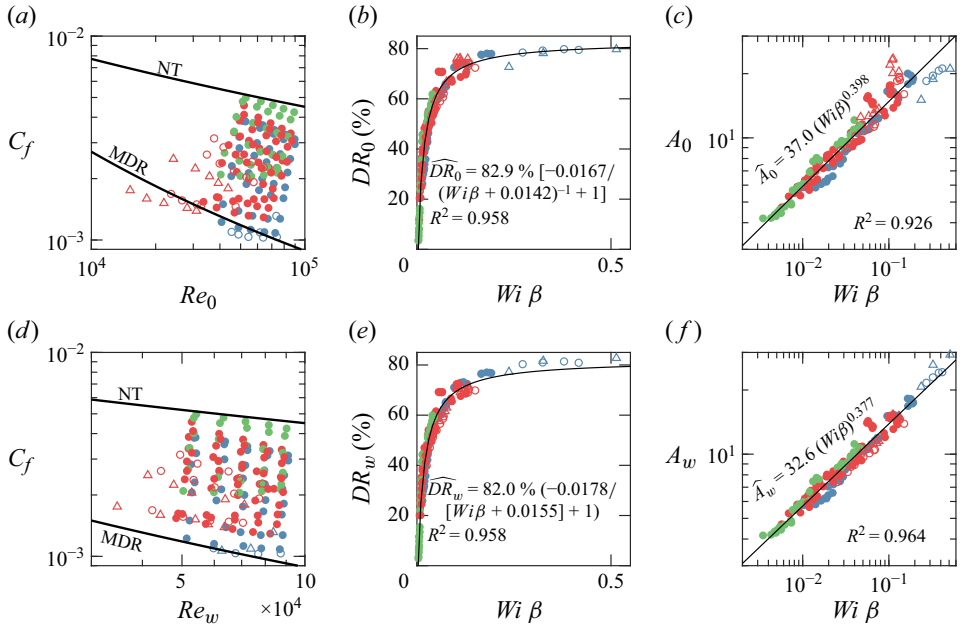

Figure 7. Plots of (*a*) C_f versus zero-shear-viscosity Reynolds number Re_0, (*b*) DR_0 based on similar Re_0 versus $Wi\beta$, (*c*) slope factor A_0 versus $Wi\beta$, (*d*) C_f versus wall-viscosity Reynolds number Re_w, (*e*) DR_w based on similar Re_w versus $Wi\beta$, (*f*) slope factor A_w versus $Wi\beta$. Lines in (*a*,*d*) labelled 'NT' correspond to Newtonian turbulence $C_f^{-1/2} = 4.0\log_{10}(ReC_f^{1/2}) - 0.4$ and 'MDR' correspond to maximum DR $C_f^{-1/2} = 19.0\log_{10}(ReC_f^{1/2}) - 32.4$ (Virk *et al.* 1970), where $Re = Re_0$ in (*a*) and $Re = Re_w$ in (*d*). Black solid lines in (*b*,*c*) and (*e*,*f*) correspond to the equations annotated on each respective panel. Marker symbols and colours are the same as those labelled in figure 4(*a*).

where C_1 is the asymptotic limit of DR as $Wi_\tau \to \infty$ and Wi_c is the critical onset value Wi_τ where DR starts to exceed 0 %. Owolabi *et al.* (2017) based (5.1) on a trend derived by Housiadas & Beris (2013) that was established using DNS with different viscoelastic constitutive models (Oldroyd-B, Giesekus and FENE-P [finitely extensible non-linear elastic dumbells with a Peterlin approximation]). The trend established by Housiadas & Beris (2013) is

$$DR = C_1\left(1 + \frac{2}{1 + \exp\left(\frac{Wi_\tau - Wi_c}{\sigma}\right)}\right), \tag{5.2}$$

where σ is a fitting constant that modifies the rate at which DR increases with Wi_τ. Note that, (5.1) from Owolabi *et al.* (2017) is the same as (5.2) from Housiadas & Beris (2013), for $\sigma = 1$ and $Wi_c = 0.5$. Figure 8 demonstrates DR as a function of the near-wall Weissenberg number Wi_τ for the present polymer drag-reduced flows. Equation (5.1) is shown in figure 8 using a dashed black line for $C_1 = 79.3$ %, which corresponds to MDR as shown in figure 5(*a*), and $Wi_c = 0.5$ from Owolabi *et al.* (2017). Measurements of DR increase with growing Wi_τ, but do not show a similar collapse on the profile of (5.1) previously seen by Owolabi *et al.* (2017). The onset Wi_τ of 0.5 appears to be consistent with Owolabi *et al.* (2017), but for all $Wi_\tau > Wi_c$ measurements deviate from (5.1). The coefficient of determination R^2 for (5.1) relative to the current measurements is 0.24, which is much worse than the R^2 of 0.820 observed by Owolabi *et al.* (2017).

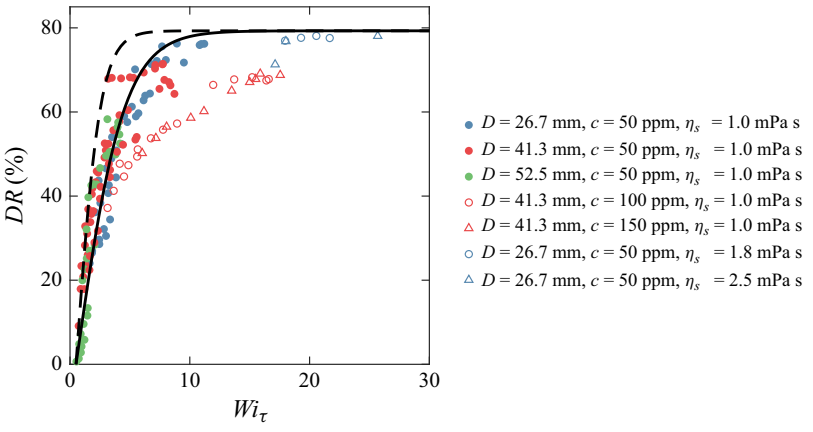

Figure 8. Drag reduction percentage based on constant $\dot{m}$ or Re_s with respect to near-wall Weissenberg number Wi_τ. The dashed black line represents the correlation of DR and Wi_τ (5.1) from Owolabi *et al.* (2017) with $C_1 = 79.3\,\%$ and $Wi_c = 0.5$. The solid black line represents the model (5.2) from Housiadas & Beris (2013) with an additional fitting parameter of $\sigma = 2$. Marker symbols and colours are the same as those presented throughout the manuscript and labelled in figure 4(*a*).

The model of (5.1) can be improved by incorporating an additional fitting parameter (σ) and utilising the trend of (5.2) proposed by Housiadas & Beris (2013). Using the same onset Weissenberg number $Wi_c = 0.5$ and asymptotic DR percentage $C_1 = 79.3\,\%$ used for (5.1), but with $\sigma = 2$, the trend in DR versus Wi_τ is much more accurately modelled, with an R^2 of 0.76. Recall that the model of Owolabi *et al.* (2017) corresponds to $\sigma = 1$; therefore, comparing the dashed and solid black lines corresponding to (5.1) and (5.2), respectively, demonstrates that increasing σ in (5.2) will delay the transition to maximum DR C_1 or reduce the rate at which DR increases with growing Wi_τ. Interestingly, much of the deviation between (5.2) corresponds to flows with larger c, despite the fact that the fluids with larger c have a more comparable β to the PAM solutions with $\beta \approx 0.1$ used in Owolabi *et al.* (2017).

One potential cause for a large error in figure 8 could be attributed to a large uncertainty in measuring $\dot{\gamma}_w$ for calculating Wi_τ. The maximum measurable shear rate $\dot{\gamma}$ in the given rheometer using the double gap Taylor–Couette geometry was approximately 200 s^{-1}. However, near-wall shear rates in the turbulent pipe flow are on the order of 10^3 to 10^4 s^{-1}, particularly for the smallest D of 26.7 mm. Extrapolating shear rheograms using shear thinning models, such as the model of Cross (1965) and given by (2.1), are typically known to produce large uncertainties in η_w and $\dot{\gamma}_w$ (Singh *et al.* 2016). Measurements of η at larger $\dot{\gamma}$ would provide better confidence in the resulting values of Wi_τ and comparison with (5.1); however, it is unclear if shear rheograms were also extrapolated in the work of Owolabi *et al.* (2017) in their derivation of $\dot{\gamma}_w$.

Another work that demonstrated scaling of C_f and DR with viscoelastic rheology was that of Chandra *et al.* (2020). In their measurements of C_f in polymer drag-reduced microtubes, Chandra *et al.* (2020) demonstrated good scaling between DR and $Wi(1-\beta)$. In the present investigation, better scaling was observed between DR and $Wi\beta$, and not $Wi(1-\beta)$, as shown in figure 5(*a*). The following discussion using figure 9 shows the discrepancy that exists if $Wi(1-\beta)$ is used.

Figure 9(*a*) demonstrates DR versus Wi for all flows. Values of DR versus Wi for different D, but a similar c of 50 ppm, tend to overlap; however, for a given DR (e.g. $DR = 50\,\%$) and D of 41.3 mm, Wi increases as c grows. Values of λ are known to increase with c (Rajesh *et al.* 2022), hence $Wi = \lambda U/D$ is expected to also increase with c for a given U

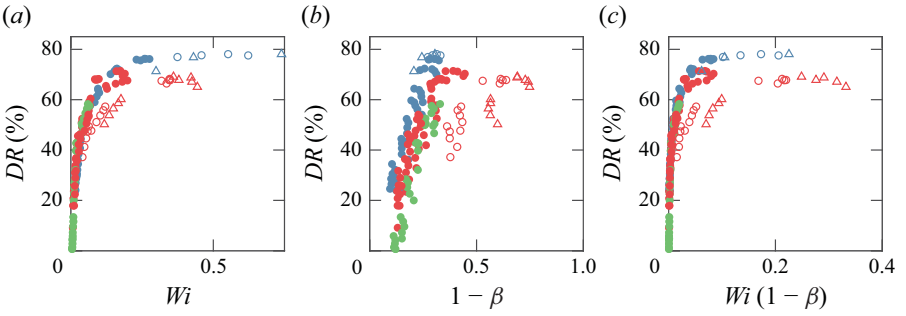

Figure 9. Drag reduction percentage based on constant $\dot{m}$ or Re_s with respect to (*a*) Wi, (*b*) $1-\beta$ and (*c*) $Wi(1-\beta)$. Marker symbols and colours are the same as those labelled in figures 4(*a*) and 8.

and D. Similarly, for a given DR, $1-\beta$ also tends to increase with c, as demonstrated by the plot of DR versus $1-\beta$ of figure 9(*b*). As shown in figure 9(*c*), multiplying Wi and $1-\beta$ does not collapse the data, as previously demonstrated by Chandra *et al.* (2020), but rather, amplifies the discrepancies between the different PAM concentrations. On the other hand, multiplying Wi with β tempers the spread in the measurements of DR for different c, as shown in figure 5(*a*). At a given DR, values of β are smaller for larger c, counteracting the spread in Wi due to concentration differences shown in figure 9(*a*). It should be noted that the present experiments are different than those of Chandra *et al.* (2020), who considered polymer drag-reduced flows with different c and polymer type, but not degraded polymer solutions. Furthermore, Chandra *et al.* (2020) does not explicitly determine λ from extensional viscosity measurements, but utilises a correlation of λ and c.

6. Further discussion

Expanding upon the discussion of figure 9, we elaborate further on the use of $Wi\beta$ as a combination of scaling parameters in the following discussion. Recall that $Wi = U\lambda/D$ represents the extent polymers are stretched within the flow (based on a bulk shear rate U/D), which is an increasing function of c. On the other hand, $\beta = \eta_s/\eta_0$ is meant to account for the influence of polymers on shear viscosity, which is a decreasing function of c. Therefore, the combination $Wi\beta$ can be interpreted as an 'effective Weissenberg number', or a viscosity corrected bulk Weissenberg number. This definition of the effective Weissenberg number ($Wi\beta$) accounts for differences in c better than other effective Weissenberg number definitions, e.g. $Wi(1-\beta)$, when predicting C_f or DR, as demonstrated when comparing figure 5(*a*) with 9(*c*).

Although the proposed model of (3.3) is able to accurately predict C_f, as shown by figure 6, its derivation is predicated on the assumption that viscoelasticity is the main contributor to DR, as stated in § 1. That said, it is possible other rheological complexities, not measured in the present investigation, could contribute to skin-friction drag or be used in lieu of λ for prediction of C_f. For example, previous investigations have demonstrated that the first normal stress differences N_1 roughly scales with DR (Escudier, Presti & Smith 1999); however, values of N_1 were also previously shown to be correlated with λ and might not imply a distinct mechanism for DR (Zell *et al.* 2010). Another rheological property that could have been considered was the extensional viscosity η_{ext}, which is widely regarded as a relevant mechanism for DR (Lumley 1973). In dimensionless terms, the ratio of the extensional to shear viscosity is the Trouton ratio $Tr = \eta_{ext}/\eta$. Measurements of η_{ext} could be implied from the present extensional rheology measurements, although strain rates are likely too low for comparison with the turbulent pipe flows. Alternatively,

the recently developed stagnation-point extensional rheology techniques could be used to derive measurements of the steady state extensional viscosity η_{ext} (Haward *et al.* 2023*a*,*b*).

7. Conclusions

To derive a functional relationship that relates the four dimensionless parameters, C_f, Wi, Re_s and β, skin-friction measurements were conducted in a pipe flow facility for 156 solutions of PAM. The experiments considered three pipe diameters and five bulk velocities, corresponding to Re_s between 60 000 and 100 000. To achieve a broad range of C_f values, the polymer solutions were also deliberately degraded using the centrifugal pump within the flow facility. This degradation influenced the rheology of the solutions, as characterised by measurements of zero-shear-rate viscosity, η_0, and elastic relaxation time, λ. Three different PAM concentrations were also considered, which further manipulated the rheology of the fluids. In addition, PAM solutions with different solvents, pure water and two glycerol/water mixtures, with unique η_s, were also examined.

Based on the experimental results, the functional relationship $C_f^{-1/2} = \widehat{A}\log_{10}(Re_s C_f^{1/2}) + \widehat{B}$, where $\widehat{A} = 27.6(Wi\beta)^{0.346}$ and $\widehat{B} = 122/15 - 58.9(Wi\beta)^{0.346}$, can be used to estimate C_f of polymer drag-reduced pipe flows given prior measurement of Wi and β using a small sample of the polymer solution. Based on this model, it is predicted that DR onset occurs when $Wi\beta$ exceeds 3.76×10^{-3}, and MDR occurs when $Wi\beta$ equals 3.40×10^{-1}. From an applied perspective, this function serves as a practical tool for predicting C_f of polymer drag-reduced pipe flows based on predefined flow features (D, U) and simple-to-measure fluid properties (ρ, η_s, η_0, λ). Future experiments should strive to confirm or correct the applicability of the derived functional relationship, by collecting similar measurements for different types of polymers (e.g. polyethylene oxide, xanthan gum), solvents (e.g. hydrocarbons), Re_s values that are beyond the range currently considered and larger D values that are more comparable to those used in industrial applications such as crude oil pipelines.

Funding. The authors acknowledge the financial support of the Natural Sciences and Engineering Research Council of Canada. The last author thanks Dr C. O'Neill for valuable discussions.

Declaration of interests. The authors report no conflict of interest.

Appendix A. Uncertainty analysis

The main source of uncertainty in $\dot{m}$ is a systematic uncertainty equal to $\pm 1.0\,\%$ of the measured $\dot{m}$, as per the Coriolis flow meter manufacturer. Random errors in mass flow rate are negligible, because $\dot{m}$ is prescribed using a controller. For measurements of ΔP, the systematic error is equal to $\pm 0.5\,\%$ of the full scale range of the pressure transducer, according to the pressure transducer manufacturer. Random uncertainties in ΔP are determined based on the repeatability of ΔP measurements for water at the five given $\dot{m}$ for each pipe D listed in table 1. For each $\dot{m}$, three repeated measurements of ΔP were collected. The random error in ΔP is taken to be the range (maximum minus minimum) in the three repeated measurements of ΔP, for each $\dot{m}$ and D. The total uncertainty in ΔP is established by taking the L2-norm between the random and systematic uncertainties, which varied between 1.2 % and 6.4 % of the average ΔP. Uncertainty in the dimensionless variables (e.g. C_f, Re_s) is determined using propagation of uncertainty (Wheeler & Ganji 2010). Figure 10(*a*) demonstrates C_f versus Re_s for water at different D. The flows at different Re_s and D show good agreement with one another, and the correlation for Newtonian turbulence $C_f^{-1/2} = 4.0\log_{10}(Re_s C_f^{1/2}) - 0.4$.

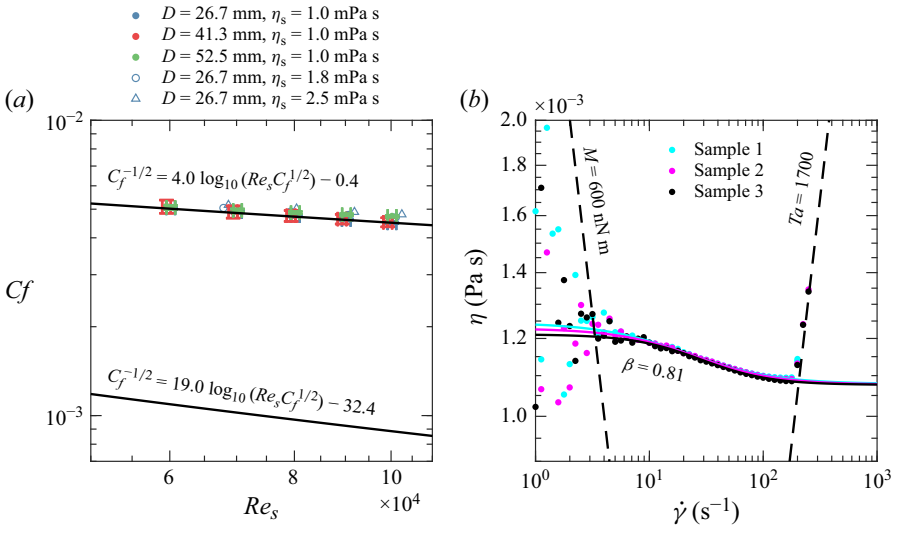

Figure 10. Plots of (*a*) C_f versus Re_s for Newtonian solvents in different pipe diameters D, and (*b*) repeated measurements of η versus $\dot{\gamma}$ for a 50 ppm PAM solution. The upper and lower black solid lines in (*a*) are the skin-friction versus Reynolds number correlations for Newtonian turbulent pipe flow and MDR (Virk *et al.* 1970), respectively. Solid lines in (*b*) represent Cross model fits according to (2.1) and dashed black lines represent the low torque ($M > 600$ nN m) and Taylor vortex ($Ta < 1700$) limits of the viscosity measurements.

The uncertainty in ΔP is assumed to be the same for the polymeric pipe flows at the given $\dot{m}$ and D listed in table 1. Among all of the polymeric and Newtonian flows the relative uncertainty in C_f varied between 2.5 % and 6.7 %. Baseline measurements of C_f versus Re_s for the Newtonian 25 % glycerol/water and 35 % glycerol/water flows in the $D = 26.7$ mm pipe are also shown on figure 10(*a*) using open symbols. Error bars in figure 10(*a*) demonstrate the uncertainties in C_f and Re_s that propagates from uncertainties in ΔP and $\dot{m}$. Properties of the flow and glycerol/water mixtures are listed in table 2. The Newtonian flows of these two glycerol/water mixtures show good agreement with measurements of water at similar Re_s and the Newtonian turbulent pipe flow correlation.

The uncertainty in η_0 was estimated considering it is an extrapolation of measurements of η to low $\dot{\gamma}$ due to the low torque limitation of the rheometer. The systematic uncertainty in η_0 is assumed to be ± 3 % of the measured η_0, as per the precision prescribed by the rheometer manufacturer. The random uncertainty in η_0 is determined based on repeated measurements of η as a function of $\dot{\gamma}$. Measurements of η versus $\dot{\gamma}$ are repeated three times for a given 50 ppm solution of PAM. The Cross model (2.1) was then fit to the three separate shear rheograms. The measurements of η versus $\dot{\gamma}$ for the three repeated samples are shown in figure 10(*b*) alongside fits using the Cross model (2.1), shown using solid lines. Measurements of η for the three samples show good repeatability for $\dot{\gamma}$ between the low torque ($M > 600$ nN m) and Taylor vortex ($Ta < 1700$) limits of the viscosity measurements, shown by the dashed black lines. Separate measurements of η versus $\dot{\gamma}$ and Cross model fits, yielded η_0 of 1.220, 1.212, 1.245 mPa s. The random uncertainty in η_0 is chosen to be the range in the measured η_0, which is equal to 0.033 mPa s or ± 2.6 % of the average η_0, for the given PAM solution. The total uncertainty was determined to be ± 4.0 % of the measured η_0, based on the L2-norm between the systematic and random uncertainties in η_0. This conservatively estimated relative error of ± 4.0 % was assumed to be the relative uncertainty of all η_0 measurements for different PAM solutions, which then propagates to errors in the dimensionless variables β.

The total uncertainty in λ is taken to be the range in the thrice-repeated measurements of λ from liquid dripping extensional rheology detailed in § 2. This uncertainty ranged between ± 1 % and ± 15 % of the average λ depending on the PAM solution. These errors in λ propagate to Wi, which is the only dimensionless parameter that depends on λ. Depending on the flow, the error in Wi varied between 1.0 % and 12.4 %.

References

Anna, S.L. & McKinley, G.H. 2001 Elasto-capillary thinning and breakup of model elastic liquids. *J. Rheol.* **45** (1), 115–138.

Arosemena, A.A., Andersson, R., Andersson, H.I. & Solsvik, J. 2021 Effects of shear-thinning rheology on near-wall turbulent structures. *J. Fluid Mech.* **925**, A37.

Buckingham, E. 1914 On physically similar systems; illustrations of the use of dimensional equations. *Phys. Rev.* **4** (4), 345–376.

Burger, E.D., Chorn, L.G. & Perkins, T.K. 1980 Studies of drag reduction conducted over a broad range of pipeline conditions when flowing prudhoe bay crude oil. *J. Rheol.* **24** (5), 603–626.

Burger, E.D., Munk, W.R. & Wahl, H.A. 1982 Flow increase in the trans alaska pipeline through use of a polymeric drag-reducing additive. *J. Petrol. Tech.* **34** (2), 377–386.

Chandra, B., Shankar, V. & Das, D. 2020 Early transition, relaminarization and drag reduction in the flow of polymer solutions through microtubes. *J. Fluid Mech.* **885**, A47.

Cross, M.M. 1965 Rheology of non-Newtonian fluids: a new flow equation for pseudoplastic systems. *J. Colloid Sci.* **20** (5), 417–437.

Deblais, A., Herrada, M.A., Eggers, J. & Bonn, D. 2020 Self-similarity in the breakup of very dilute viscoelastic solutions. *J. Fluid Mech.* **904**, R2.

Escudier, M.P., Presti, F. & Smith, S. 1999 Drag reduction in the turbulent pipe flow of polymers. *J. Non-Newtonian Fluid Mech.* **81** (3), 197–213.

Goudar, C.T. & Sonnad, J.R. 2003 Explicit friction factor correlation for turbulent flow in smooth pipes. *Ind. Engng Chem. Res.* **42** (12), 2878–2880.

Haward, S.J., Pimenta, F., Varchanis, S., Carlson, D.W., Toda-Peters, K., Alves, M.A. & Shen, A.Q. 2023*a* Extensional rheometry of mobile fluids. Part I: OUBER, an optimized uniaxial and biaxial extensional rheometer. *J. Rheol.* **67** (5), 995–1009.

Haward, S.J., Varchanis, S., McKinley, G.H., Alves, M.A. & Shen, A.Q. 2023*b* Extensional rheometry of mobile fluids. Part II: comparison between the uniaxial, planar, and biaxial extensional rheology of dilute polymer solutions using numerically optimized stagnation point microfluidic devices. *J. Rheol.* **67** (5), 1011–1030.

Housiadas, K.D. & Beris, A.N. 2013 On the skin friction coefficient in viscoelastic wall-bounded flows. *Intl J. Heat Fluid Flow* **42**, 49–67.

Lumley, J.L. 1973 Drag reduction in turbulent flow by polymer additives. *J. Polym. Sci.* **7** (1), 263–290.

Owolabi, B.E., Dennis, D.J.C. & Poole, R.J. 2017 Turbulent drag reduction by polymer additives in parallel-shear flows. *J. Fluid Mech.* **827**, R4.

Pereira, A.S. & Soares, E.J. 2012 Polymer degradation of dilute solutions in turbulent drag reducing flows in a cylindrical double gap rheometer device. *J. Non-Newtonian Fluid Mech.* **179**, 9–22.

Rajesh, S., Thiévenaz, V. & Sauret, A. 2022 Transition to the viscoelastic regime in the thinning of polymer solutions. *Soft Matt.* **18** (16), 3147–3156.

Savins, J.G. & Seyer, F.A. 1977 Drag reduction scale-up criteria. *Phys. Fluids* **20** (10), S78–S84.

Singh, J., Rudman, M. & Blackburn, H.M. 2017 The influence of shear-dependent rheology on turbulent pipe flow. *J. Fluid Mech.* **822**, 848–879.

Singh, J., Rudman, M., Blackburn, H.M., Chryss, A., Pullum, L. & Graham, L.J.W. 2016 The importance of rheology characterization in predicting turbulent pipe flow of generalized Newtonian fluids. *J. Non-Newtonian Fluid Mech.* **232**, 11–21.

Soares, E.J., Sandoval, G.A.B., Silveira, L., Pereira, A.S., Trevelin, R. & Thomaz, F. 2015 Loss of efficiency of polymeric drag reducers induced by high Reynolds number flows in tubes with imposed pressure. *Phys. Fluids* **27** (12), 125105.

den Toonder, J.M.J., Draad, A.A., Kuiken, G.D.C. & Nieuwstadt, F.T.M. 1995 Degradation effects of dilute polymer solutions on turbulent drag reduction in pipe flows. *Appl. Sci. Res.* **55** (1), 63–82.

Virk, P.S. 1975 Drag reduction fundamentals. *AIChE J.* **21** (4), 625–656.

Virk, P.S., Mickley, H.S. & Smith, K.A. 1970 The ultimate asymptote and mean flow structure in Toms' phenomenon. *ASME J. Appl. Mech.* **37** (2), 488–493.

WHEELER, A.J. & GANJI, A.R. 2010 *Introduction to Engineering Experimentation*. 3rd edn. Pearson Higher Education.

WHITE, C.M. & MUNGAL, M.G. 2008 Mechanics and prediction of turbulent drag reduction with polymer additives. *Annu. Rev. Fluid Mech.* **40** (1), 235–256.

XI, L. 2019 Turbulent drag reduction by polymer additives: fundamentals and recent advances. *Phys. Fluids* **31** (12), 121302.

ZELL, A., GIER, S., RAFAI, S. & WAGNER, C. 2010 Is there a relation between the relaxation time measured in CaBER experiments and the first normal stress coefficient? *J. Non-Newtonian Fluid Mech.* **165** (19–20), 1265–1274.